

Time-Optimal Quantum Driving by Variational Circuit Learning

Tangyou Huang,^{1,2} Yongcheng Ding,¹ Léonce Dupays,³ Yue Ban,⁴ Man-Hong Yung,^{5,6,7} Adolfo del Campo,^{3,8} and Xi Chen^{1,9}

¹*Department of Physical Chemistry, University of the Basque Country UPV/EHU, Apartado 644, 48080 Bilbao, Spain*

²*International Center of Quantum Artificial Intelligence for Science and Technology (QuArtist)
and Department of Physics, Shanghai University, 200444 Shanghai, China*

³*Department of Physics and Materials Science, University of Luxembourg, L-1511 Luxembourg, Luxembourg*

⁴*TECNALIA, Basque Research and Technology Alliance (BRTA), 48160 Derio, Spain*

⁵*Central Research Institute, 2012 Labs, Huawei Technologies, Shenzhen 518129, China*

⁶*Department of Physics, Southern University of Science and Technology, Shenzhen 518055, China*

⁷*Shenzhen Institute for Quantum Science and Engineering,*

Southern University of Science and Technology, Shenzhen 518055, China

⁸*Donostia International Physics Center, E-20018 San Sebastián, Spain*

⁹*EHU Quantum Center, University of the Basque Country UPV/EHU, Barrio Sarriena, s/n, 48940 Leioa, Spain*

(Dated: November 2, 2022)

The simulation of quantum dynamics on a digital quantum computer with parameterized circuits has widespread applications in fundamental and applied physics and chemistry. In this context, using the hybrid quantum-classical algorithm, combining classical optimizers and quantum computers, is a competitive strategy for solving specific problems. We put forward its use for optimal quantum control. We simulate the wave-packet expansion of a trapped quantum particle on a quantum device with a finite number of qubits. We then use circuit learning based on gradient descent to work out the intrinsic connection between the control phase transition and the quantum speed limit imposed by unitary dynamics. We further discuss the robustness of our method against errors and demonstrate the absence of barren plateaus in the circuit. The combination of digital quantum simulation and hybrid circuit learning opens up new prospects for quantum optimal control.

I. INTRODUCTION

Following the vision by Feynman [1], quantum simulation has acquired a potentially-disruptive role in the development of contemporary science and technology, given the prospects of harnessing the advantage of using a quantum computer (QC) for specific applications. In recent decades, quantum simulation has been used to probe the dynamics of condensed matter systems [2, 3], for quantum chemistry [4, 5], and as a test-bed for nonequilibrium statistical mechanics, e.g., in studying thermalization and nonequilibrium behavior of many-body systems [6, 7]. Quantum simulation is also expected to impact high-energy physics, given the potential to facilitate the study of lattice gauge theories [8] and gauge-gravity duality [9, 10], among other examples.

The use of a digital quantum simulator (DQS) based on the gate model offers a prominent approach in current Noisy Intermediate-Scale Quantum (NISQ) devices [11] and has gained relevance with theoretical and experimental progress [12–14]. In particular, DQS can be used to implement variational quantum algorithms (VQAs), under development for quantum optimization [15], quantum machine learning [16], and quantum control [17]. Their formulation generally approximates the continuous time evolution by discrete, finite Trotter steps [18–21] implemented by a sequence of quantum gates, with controlled accuracy, in principle. However, balancing the number of Trotter steps and imperfections of quantum circuits in experiments is still a fundamental challenge. In this sense, various optimization scenarios aim at quantum error mitigation [22–24] for achieving a good precision of the quantum simulation with limited quantum resources. Among those, the machine-learning-enhanced optimization protocol [25–28] utilizes a feedback loop between the quantum device

and a classical optimizer. This approach is particularly useful in the field of hybrid quantum algorithms [29, 30] with current quantum hardware. Nonetheless, solving the quantum optimal control problem by VQAs in a NISQ device is still an open challenge [17].

In this work, we propose a circuit learning scheme based on gradient-descent (GD) for time-optimal quantum control. As a concrete example, we consider a quantum particle trapped in time-varying parabolic potential. We use a qubit register and encode the spatial wave function using the basis of n -qubit states. We then reproduce the exact state evolution on a designed quantum circuit using a digital algorithm [31, 32]. We optimize the control function to achieve maximum-fidelity control by using the GD-based circuit learning. We further unveil the connection between a control phase transition and the quantum speed limit, i.e., the minimum time for a quantum state to evolve into a distinguishable state under a given dynamics. We demonstrate that the fidelity-based GD method avoids a large number of measurements by comparison to the reinforcement learning protocol [33] and show how it can be accelerated by choosing different quantum quantities as the cost function.

In the following two sections, we introduce the quantum algorithm for the circuit realization of a quadratic Hamiltonian and discuss the time-dependent harmonic oscillator as an example. We then explore a fidelity-based GD method for maximum-fidelity control in a nonequilibrium expansion process and characterize the efficiency through various cost functions. The relation of the quantum speed limit to the control phase transition is then discussed. Finally, we establish the fault tolerance of our method against the quantum errors in experiments and also address the problem of barren plateaus in the parameterized circuit.

II. PRELIMINARIES AND NOTATION

A. Time-dependent quantum harmonic oscillator

We exemplify our approach by considering the time-dependent harmonic oscillator (TDHO), described by the Hamiltonian

$$H(t) = \frac{\hat{p}^2}{2m} + \frac{1}{2}m\omega^2(t)[\hat{x} - x_0(t)]^2, \quad (1)$$

where $\omega(t)$ and $x_0(t)$ are tunable and represent the trap frequency and the location of the trap center, respectively. The TDHO is an ideal model for benchmarking quantum control algorithms since its dynamics admits exact closed-form solutions. In particular, we focus on the case with $x_0(t) = 0$ and look for the expansion of the wave packet induced by a modulation of the trap frequency $\omega(t)$ from an initial value ω_0 to a final one ω_f . This model has many applications, including the cooling of a particle in an optical trap [34], mechanical resonators [35], and tunable transmon superconducting qubits [36]. The ground state of $H(0)$ evolves into the time-dependent Gaussian state [34]

$$\begin{aligned} \Psi(t, x) = & \left(\frac{m\omega_0}{\pi\hbar b^2}\right)^{1/4} \exp\left[-\frac{i}{2}\int_0^t \frac{\hbar\omega_0}{b^2} dt'\right] \\ & \times \exp\left[\frac{im}{2\hbar}\left(\frac{\dot{b}}{b} + i\frac{\omega_0}{b^2}\right)x^2\right], \end{aligned} \quad (2)$$

where the time-dependent scaling factor $b(t) > 0$ characterizes the width of the wave packet and satisfies the auxiliary equation

$$\ddot{b} + \omega^2(t)b = \frac{\omega_0^2}{b^3}. \quad (3)$$

A primary numerical solver of quantum dynamics is the so-called *split-operator method* (SOM), also known as the split time propagation scheme [37]. For the sake of convenience, one usually sets dimensionless variables based on physical units of energy $\epsilon = \hbar\omega_0$, length $b_{\text{HO}} = \sqrt{\hbar/m\omega_0}$, and time $\tau = 1/\omega_0$. In a classical computer, one defines a N -dimensional vector as $\Psi(\mathbf{r})$ for encoding the amplitude of the wave function on the space grid $\mathbf{r} = [x_0, x_1, \dots, x_{N-1}]$. Note that the kinetic energy operator $\hat{T} = \hat{p}^2/2$ and the potential operator $\hat{V} = \omega^2(t)\hat{x}^2/2$ do not commute. Thus, the following approximation stands for small dt with an error $\mathcal{O}(dt^3)$

$$e^{-iHdt} \approx e^{-\frac{i}{2}\hat{V}dt} e^{-i\hat{T}dt} e^{-\frac{i}{2}\hat{V}dt}, \quad (4)$$

evolving the wave function in a Trotter step. A common trick in implementing this method uses forward and inverse Fourier transforms to change the representation of the quantum state between the real space \mathbf{r} and momentum space \mathbf{k} , in which the kinetic energy operator becomes diagonal in \mathbf{k} , simplifying the numerical calculation.

B. Time-optimal control

The frictionless expansion of quantum particles trapped in a time-varying harmonic trap can be formulated as a time-optimal control problem by minimizing the time of the process t_f [34, 38–41]. It follows from Pontryagin's maximum principle that the control Hamiltonian for all $t \in [0, t_f]$ takes the form [38]

$$H_c[x_1, x_2, p_1, p_2] = p_1x_2 + \frac{p_2}{x_1^3} - p_2x_1u(t), \quad (5)$$

where the state $x_1 = b$, $x_2 = \dot{b}/\omega_0$, and the controller $u(t) = \omega^2(t)/\omega_0^2$ are governed by the Ermakov equation (3). Here, p_1 and p_2 are the conjugate momentum of x_1 and x_2 , respectively. Substituting the control Hamiltonian into the canonical equation leads to the cost equations

$$\dot{p}_1 = \left(u + \frac{3}{x_1^4}\right)p_2, \quad (6)$$

$$\dot{p}_2 = -p_1. \quad (7)$$

If the controller is bounded as $\delta_1 \leq u(t) \leq \delta_2$, the time-optimal control has a bang-bang form, i.e., it is a piece-wise function and constant in each interval. For a specific problem with $b(0) = 1$ and $b(t_f) = \sqrt{\omega_0/\omega_f} = \gamma$, consider the feasible three-jump protocol

$$u(t) = \begin{cases} 1 & t = 0 \\ \delta_1 & 0 < t \leq t_1 \\ \delta_2 & t_1 < t < t_1 + t_2 \\ 1/\gamma^4 & t = t_f^{\text{opt}} = t_1 + t_2 \end{cases}, \quad (8)$$

where the switching time t_1 and the optimal operation time $t_f^{\text{opt}} = t_1 + t_2$ can be calculated by integrating the Ermakov equation (3) by using boundary conditions. This yields the closed-form exact time-optimal driving protocol $u(t)$ with

$$\begin{aligned} t_1 &= \frac{1}{\sqrt{\delta_1}} \sinh^{-1} \sqrt{\frac{\delta_1(\gamma^2 - 1)(\gamma^2\delta_2 - 1)}{(\delta_1 - \delta_2)\gamma^2(1 - \delta_1)}}, \\ t_2 &= \frac{1}{\sqrt{\delta_2}} \sin^{-1} \sqrt{\frac{\delta_2(\gamma^2 - 1)(1 - \gamma^2\delta_1)}{(\delta_1 - \delta_2)(1 - \gamma^4\delta_2)}}. \end{aligned} \quad (9)$$

C. Quantum speed limit

Quantum speed limits (QSLs) provide fundamental upper bounds on the speed of quantum evolution [42]. They have wide-spread applications ranging from quantum metrology to optimal control [43–45]. QSLs are formulated by choosing a notion of distance between quantum states and identifying a maximum speed of evolution. For isolated systems described by a time-independent Hamiltonian, two seminal results are known. The Mandelstam-Tamm QSL determines the maximum speed of evolution in terms of the energy dispersion [46], while the Margolus-Levitin bound uses the mean energy

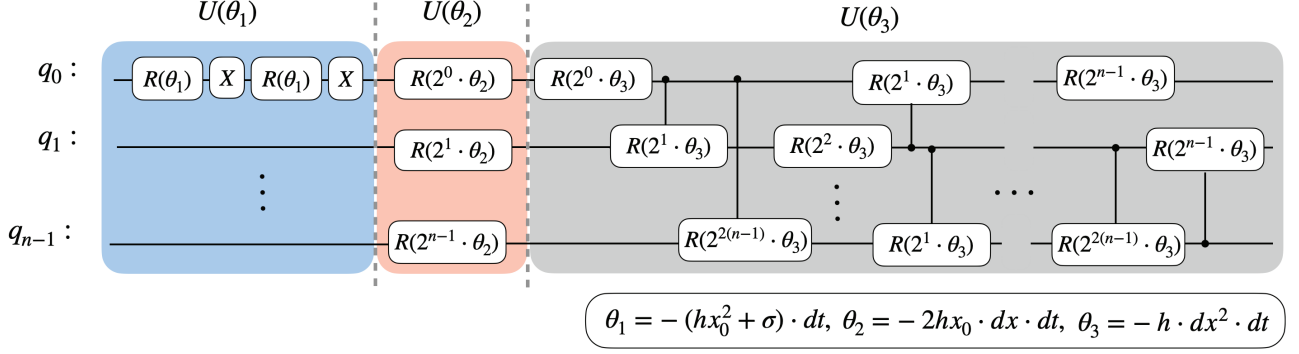


FIG. 1. The circuit realization of time-evolution operator for a quadratic Hamiltonian as defined by Eq. (22). The single phase gate and Pauli-X gate are schematically represented by the symbols $R(\cdot)$, X , and the corresponding control gates are shown by vertical lines with black circles.

above the ground state instead [47]. The interplay of these bounds has recently been demonstrated in a trapped system made of ultracold atoms that are suddenly quenched [48]. For a generic driven system, only an analog of the Mandelstam-Tamm bound is known [49–51].

Consider the quantum unitary dynamics generated by a time-dependent Hamiltonian according to the Schrödinger equation. The distance between the initial state and the time-dependent state in projective Hilbert space can be quantified by the Bures angle

$$\mathcal{L}(\psi_0, \psi_t) = \arccos(|\langle \psi_0 | \psi_t \rangle|) \in [0, \pi/2]. \quad (10)$$

The minimum time scale required to sweep a given Bures angle is lower bounded by

$$\tau_{\text{QSL}} = \frac{1}{\overline{\Delta E}} \mathcal{L}(\psi_0, \psi_t), \quad (11)$$

where the speed of evolution is set by the time-averaged energy dispersion

$$\overline{\Delta E} = \frac{1}{t} \int_0^t ds \sqrt{\langle \psi_s | \hat{H}(s)^2 | \psi_s \rangle - \langle \psi_s | \hat{H}(s) | \psi_s \rangle^2}. \quad (12)$$

The QSL τ_{QSL} is thus approached by maximizing the energy dispersion at all times. In control protocols for wave-packet expansion, we consider the evolution of the ground state of the trap with initial trapping frequency ω_0 to the ground state of the trap with final frequency ω_f . Provided that the control protocol, specified by $u(t)$, has unit efficiency in preparing the target state, the Bures angle is fixed, and the corresponding QSL reads

$$\tau_{\text{QSL}} = \frac{\hbar}{\overline{\Delta E}} \sqrt{\frac{2\gamma}{1 + \gamma^2}}. \quad (13)$$

We note that τ_{QSL} should be distinguished from the minimum time t_f^{opt} in the preceding time-optimal control with the trap frequency bounded.

D. Fidelity susceptibility

Generally, the final state $\rho_f = |\Psi_f(x)\rangle\langle\Psi_f(x)|$ upon completion of a control protocol at $t = t_f$ differs from the target state $\rho_{\text{tar}} = |\Psi_{\text{tar}}(x)\rangle\langle\Psi_{\text{tar}}(x)|$ one wishes to prepare. Let us consider the fidelity F between these two states

$$F(\rho_{\text{tar}}, \rho_f) = \left[\text{Tr}(\sqrt{\sqrt{\rho_{\text{tar}}}\rho_f\sqrt{\rho_{\text{tar}}}}) \right]^2, \quad (14)$$

where $\text{Tr}(\cdot)$ denotes the trace operation.

The *fidelity susceptibility* χ_f quantifies the fidelity response to a slight change of driving parameter [52–54]. For a functional Hamiltonian $H(f_t)$ parameterized by f_t , let $|\Psi_0(f_t)\rangle$ be the ground state. We assume f_t to be a function of time and consider a variation on the control function $f_t \rightarrow f_t + \delta f$, where $\delta f \rightarrow 0$ is small enough to apply perturbation theory. As a result, the perturbed ground state is $|\Psi_0(f + \delta f)\rangle$. The fidelity susceptibility, without loss of generality, is defined as

$$\chi_f \equiv \frac{-2 \ln(F_{\delta f})}{\delta f}, \quad (15)$$

where the fidelity $F_{\delta f} = F[\rho_0(f), \rho_0(f + \delta f)]$. The *fidelity susceptibility* quantifies the sensitivity of the fidelity to variations of the control functions. In other words, the fidelity susceptibility can be used as a cost function to accelerate the convergence of the optimization process. For the sake of simplicity, we assume that $\delta f \rightarrow 0$ is a time-independent real value.

III. QUANTUM CIRCUIT REALIZATION OF QUADRATIC HAMILTONIAN

Next, we present the algorithm for the circuit realization of quadratic Hamiltonians using a finite set of elementary quantum gates. We focus on DQS of the continuous-variables system and encode a wave packet onto a n -qubit register. Quan-

tum states of this register can be described in binary notation

$$|\Phi\rangle = \sum_{i=0}^{2^n-1} c_i |i\rangle, \quad (16)$$

using the computational basis $|i\rangle = |q_{n-1}\rangle \otimes \dots \otimes |q_1\rangle \otimes |q_0\rangle$ with $q_0, q_1, \dots, q_{n-1} \in \{0, 1\}$, and the corresponding amplitudes c_i normalized as $\sum_{i=0}^{2^n-1} |c_i|^2 \equiv 1$. To solve the time-dependent Schrödinger equation on a quantum computer with a n -qubit register, we discretize the continuous variables associated with the spatial coordinate x and time t , and subsequently map the coordinate space x into the Hilbert space of n qubits. Specifically, the compact continuous spatial domain $x \in [-L, L]$ is approximated by a lattice of 2^n points spaced by a constant interval $dx = L/(2^{n-1} - 1)$. A wave packet can be encoded in the state of the n -qubit register as

$$|\Phi\rangle = \sum_{i=0}^{2^n-1} \Psi(x_i) |i\rangle \quad (17)$$

$$= \Psi(x_0) |0 \dots 0\rangle + \dots + \Psi(x_{2^n-1}) |1 \dots 1\rangle, \quad (18)$$

which reproduces the vectorized wave function for the following quantum analog of the SOM in the Hilbert space. As in numerical discretization methods, this encoding of $\Psi(\mathbf{r})$ provides, in principle, satisfactory accuracy when the lattice length dx is much smaller than any characteristic length scale of the wave packet. The preparation of arbitrary initial qubit states $|\Phi\rangle$ based on the initialized wave-packet $\Psi(\mathbf{r})$ can be approached by the variational quantum eigensolver (VQE)

$$|\tilde{\Phi}\rangle = \prod_{i=1}^p \left[\prod_{q=0}^{n-1} (U^{q,i}) U_{\text{ENT}} \right] |+\rangle^{\otimes n}, \quad (19)$$

where $|+\rangle = \frac{1}{\sqrt{2}}(|0\rangle + |1\rangle)$ is a single-qubit state, the unitary $U^{q,i}(\theta) = R_z^{q,i}(\theta_1^{q,i}) R_x^{q,i}(\theta_2^{q,i}) R_z^{q,i}(\theta_3^{q,i})$ is a universal single-qubit gate, and U_{ENT} represents CNOT gates that entangle the neighboring qubits with periodic boundary conditions. In this way, an approximated initial state $|\tilde{\Phi}\rangle$ is prepared by optimizing $3pn$ parameters to minimize the cost function.

Next, consider the digital quantum simulation aimed at reproducing an equivalent SOM. The dynamics of the wave packet is described by

$$\Phi(t + dt) \approx e^{-iH(t)dt} \Phi(t), \quad (20)$$

where e^{-iHdt} is the time-evolution operator for the time step dt .

We use the quantum Fourier transform (QFT) as the quantum analog of the inverse discrete Fourier transform, which is key to the efficient implementation of the SOM. Hence, the wave function $|\Phi\rangle$ is evolved as

$$|\tilde{\Phi}(t + dt)\rangle = \mathcal{V}(t)_{dt/2} \text{QFT} \mathcal{T}(t)_{dt} \text{QFT}^\dagger \mathcal{V}(t)_{dt/2} |\tilde{\Phi}(t)\rangle, \quad (21)$$

where $\mathcal{V}(t)$ and $\mathcal{T}(t)$ are the potential operator and the kinetic-energy operator in the real space and momentum space, respectively. In other words, they are both quadratic, and their diagonal elements can be written as

$$A_{jj} = \exp \left\{ -idt [h(jdx + x_0)^2 + \sigma] \right\}, \quad (22)$$

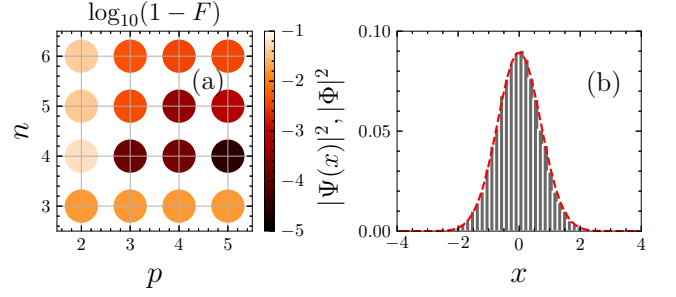


FIG. 2. The fidelity of states preparation by VQE as a function of qubit number n and parameter depth p in (a), and corresponding probability distribution of qubits $|\Phi|^2$ compared with density of wave function $|\Psi(x)|^2$ in (b), with fidelity $F = 0.996$ for $n = 6$ and $p = 4$.

where other off-diagonal elements are zero. The preliminary result in Ref. [31] demonstrates that the quadratic Hamiltonian can be exactly decomposed into a quantum circuit. In Fig. 1, we plot the quantum circuit for implementing a quadratic Hamiltonian in the computational basis for DQS. The decomposition is verified by the DQS of nonadiabatic processes in molecular systems [32].

IV. FIDELITY-BASED GRADIENT DESCENT

A. Initial state preparation

The first step is to encode the information of the wave packet into the state of the qubit register. The accuracy of the preparation of a target state of qubits by VQE depends on the qubit number n and the parameter depth p , see Eq. (19). As we know, the depth p and qubit number n exponentially increase the complexity of VQE. In Fig. 2, we compare the fidelity of state preparation in the coefficient grid n, p in (a). In (b), without loss of accuracy, we choose $n = 6$, $p = 4$, and present the resulting n -qubits states for the corresponding density (2) with $\omega_0 = 1$. In what follows, the numerical results are produced by the quantum simulator `statevector simulator` on the `qiskit` platform, which admits no errors, decoherence, and imperfections at all. We will consider the noise of an actual quantum device in the discussion.

B. The maximum-fidelity control

A parametric optimization problem is usually mapped into the minimization of a given cost function to find its local minimum with the Gradient Descent (GD) algorithm. The optimal solution $M = \{m_0, m_1, \dots, m_i\}$ is obtained by minimizing the cost-value $c = J(M)$, and can be expressed as

$$M^{\text{opt}} = \min_c J(M). \quad (23)$$

In our case, the control function is the trap frequency $f(t) = \omega^2(t)$ that is piece-wise on the discrete time $t \in [0, t_f]$ in-

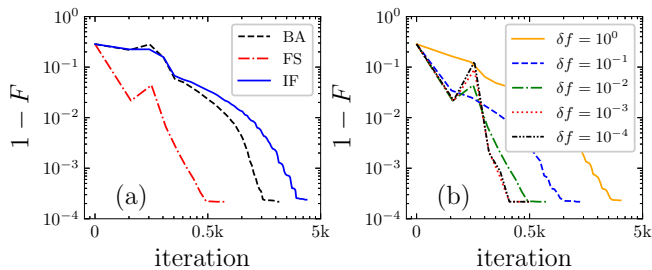


FIG. 3. (a) The infidelity $1 - F$ as a function of the training iteration using three different loss functions: fidelity susceptibility (FS) with $\delta f = 0.01$, infidelity (IF), and Bures angle (BA). (b) The infidelity as a function of the iteration step for different δf is compared when the fidelity susceptibility (FS) is taken as a loss function. Parameters: $N_t = 50$, $\omega_f = 0.1$, $n = 6$, $p = 4$, $\delta_1 = 10^{-6}$, $\delta_2 = 1$, and $t_f = 3.152$.

volving N_t -intervals. Accordingly, the control tuple $f(t) = \{f(0), f(dt), \dots, f(t_f)\}$ is constrained by $\delta_1 \leq |f(t)| \leq \delta_2$, $|f(t+dt) - f(t)| \leq \Delta f$ and the boundary conditions $f(0) = 1$ and $f(t_f) = 0.01$ are considered for trap expansion with $\omega_f/\omega_0 = 1/10$. Then, we optimize ω -dependent parameters $M = \{\theta_3(\omega)\}_t$ in the circuit shown in Fig. 1 by minimizing the loss value which can be generated by the measurements on the qubits at $t = t_f$. Here, we exploit three different cost functions: the infidelity (IF) ($1 - F$), the fidelity susceptibility (FS) χ_f , and the Bures angle $\mathcal{L}(\psi_t, \psi_{\text{tar}})$. For simplicity, we initialize the controller $f(t)$ with a linear dependence of the form $f(t) = (\omega_f^2 - \omega_0^2)(t/t_f) + \omega_0^2$. This yields a parametric constrained minimization problem in this case. We exemplify the optimization process of finding maximum-fidelity policy for different cost functions in Fig. 3 by using the optimizer SLSQP [55] based on the `scipy` [56] platform. To this end, we assign the total time $t_f = t_f^{\text{opt}}$ calculated in (9), and use the GD method to minimize the cost function for obtaining the maximum-fidelity control function. In Fig. 3, we present infidelities versus the GD iteration when using each cost function. The control with maximum fidelity is obtained with their convergence. One can see that the learning rate of FS outperforms the others with the same optimizer in (a), and we compare the FS-based GD with various coefficients: $\delta f = [10^{-4}, 10^{-3}, 10^{-2}, 10^{-1}, 10^0]$ in (b). Because the greatest convergent rate of the optimization process arises when $\delta f \leq 10^{-3}$, we employ the FS χ_f as the cost function with the coefficient $\delta f = 10^{-3}$ to design the maximum fidelity policy in the GD algorithm. It is worth emphasizing that reducing the training iteration is equivalent to decreasing the accumulation of operation errors. As a result, we can improve the accuracy of DQS with the same quantum volume.

By considering the trade-off between the complexity and accuracy of digitized circuits, we analyze the fidelity achieved by the maximum-fidelity policy for different numbers of Trotter steps N_t and the constraints on control step Δf . Trotter steps N_t and the constraints on control step Δf determine the depth of the circuit and the continuity of the control function, respectively. In Fig. 4, we present the fidelity density as a function of N_t and Δf in (a) and show the maximum-

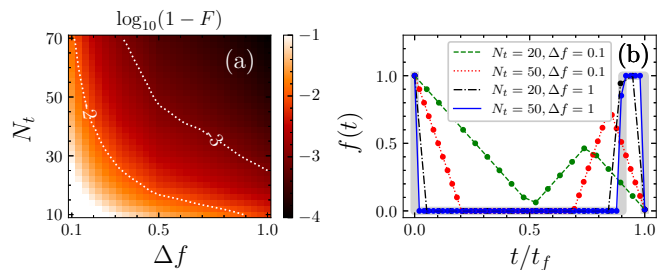


FIG. 4. (a) Fidelity as function of Δf and N_t with total time $t_f = 3.152$. The two dashed contour curves refer to $F = 0.99, 0.999$ and are labeled by $-2, -3$, respectively. In (b), we present the trained fidelity-optimal controls compared to the bang-bang control (solid gray line). The fidelity takes values $F = 0.84, 0.98, 0.998, 0.9998$ in the four cases illustrated in the legend from top to bottom. Other parameters are chosen as in Fig. 3

fidelity control protocols for various N_t and Δf , where the counter curves corresponding to the fidelity $F = 0.999, 0.99$ are marked. In addition, in Fig. 4(b), the results from circuit learning are compared with the the optimal-time protocol $t_f = t_f^{\text{opt}}$ produced by bang-bang control (8). The higher accuracy of DQS requires the larger Trotter step N_t and higher computation complexity. On the other hand, the control function becomes smoother when $\Delta f \rightarrow 0$, with increasing the Trotter step and circuit complexity. In this context, we choose $N_t = 50$ and $\Delta f = 1$ in the following calculations.

C. Control phase transition at quantum speed limit

In the previous section, we described an efficient GD-based hybrid algorithm to find the maximum-fidelity control in a quantum device by considering the loss function J , Trotter step N_t , and step length Δf . Next, we shall prove the control phase transition (CPT) appears at the critical point due to the QSL. The use of optimal control to reach the QSL in quantum state manipulation has been discussed in [43]. However, the authors in [43] intended to find maximum fidelity control by reducing infidelity, which is a highly time-consuming task. This can be improved by introducing the fidelity susceptibility χ , as we have shown in the previous section. In the space of protocols, the control phase transition is associated with abrupt changes in an optimal control function, satisfying given constraints as the duration of the process is varied [33]. In particular, the maximum-fidelity control function is unique when $t \leq t^{\text{opt}}$. It is expected that the QSL can be reached at the point of CPT.

In practice, we consider the expansion process: from initial state ψ_0 ($\omega_0 = 1$) to target states ψ_{tar} ($\omega_f = 0.1$) with constrain $\delta_1 = 10^{-6}$, $\delta_2 = 1$ by assuming $\omega^2(t) > 0$, and subsequently generate the maximum-fidelity control sequence $f(t)$ for $t_f \in [2, 5]$, where other parameters are same as those in Fig. 3. Consequently, we present the control phase diagram in Fig. 5(a) and illustrate several control functions of selected t_f compared with the optimal bang-bang control (8). The con-

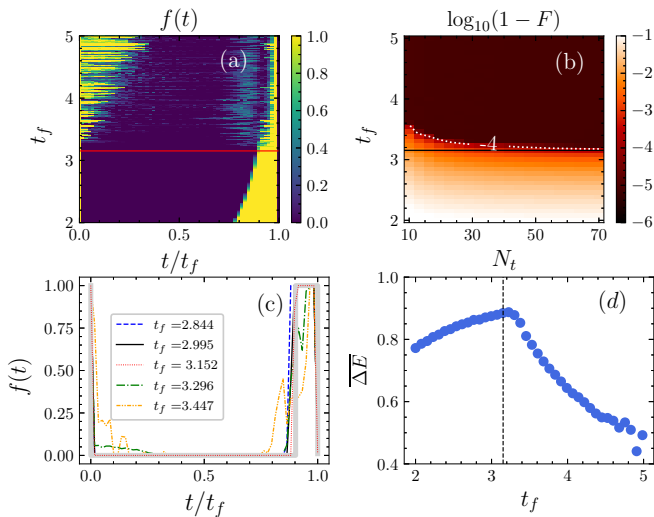


FIG. 5. (a) The control phase diagram, with the fidelity-optimal control sequence $f(t) = \omega^2(t)$ as a function of t/t_f for different $t_f \in [2, 5]$. (b) Logarithm of the infidelity $\log_{10}(1-F)$ as a function of t/t_f , N_t . The solid line is included as a reference in (a) and (b) and corresponds to the optimal bang-bang control with $t_f^{\text{opt}} = 3.152$. (c) The trained fidelity-optimal controls for different values of the total time t_f are compared with the optimal bang-bang control, (thick gray line). (d) The corresponding time-averaged energy dispersion ΔE for maximum-fidelity control. Parameters agree with those in Fig. 3.

control function is suddenly converted to a non-bang-bang-typed phase at the transition point $t_f \approx t_f^{\text{opt}}$, i.e., the control phase transition point. In addition, we note that there exists only one solution of the maximum-fidelity control function when $t_f \leq t_f^{\text{opt}}$ for fulfilling the requirement of time-energy bound (11). Here, we confirm the minimum time t_f^{min} when the maximum-fidelity is larger than 0.999, and compare the result for different N_t in (b) of Fig. 5. It is evident in Fig. 5(c) that the accuracy of optimal time produced by circuit learning essentially depends on the N_t , and we set $N_t = 50$ for the criteria of $\log_{10}(1-F) \sim -4$ in the following calculations.

We emphasize that the time-optimal driving obtained here differs from the QSL but is closely related to it. Specifically, the time-optimal driving is bounded in terms of the trap frequency by contrast to the QSL, which is bounded in terms of the time-averaged standard deviation of the energy, see Eq. (13). The former is a weaker and more conservative bound, as the energy fluctuations can be upper-bounded in terms of the frequency. In Fig. 5(d), we display the energy dispersion of maximum-fidelity control and compare it with the corresponding time-optimal driving. The energy dispersion becomes consistently unique when $t_f \leq t_f^{\text{opt}}$ before the point of CPT. Moreover, the energy dispersion for the maximum fidelity control is slightly smaller than in the time-optimal bang-bang control with bounded trap frequency. In this sense, one can approach the QSL in time-optimal driving when an additional energy cost is allowed by relaxing the trap frequency bound.

V. DISCUSSION

A significant source of discussion is the robustness of VQAs in an environment with stochastic perturbations. In a real quantum computer with NISQ hardware, imperfections are unavoidably induced as a result of a finite number of measurements and a noisy environment. As emphasized, the previous results are produced by the quantum simulator statevector simulator in the qiskit platform, with no errors, decoherence, and imperfections at all. In this section, we implement our method in a noise-associated quantum device simulated by qasm simulator with N_m measurement shots. The performance of the GD algorithm depends on the tolerance of the optimizer to errors. Thus, we shall balance the GD induced by noise and the parameter variance in a training landscape. Let us recall the definition of noise in the framework of quantum information processing. In general, the n -qubits register is coupled with an environment ε , leading to the nonunitary evolution of the system. Initially, we assume the density operators of the register $\rho(t_0) = \rho_0$ and the environment to be decoupled so that the composite state is given by the tensor product $\rho \otimes \varepsilon$. For any global unitary operator U describing the dynamics of the composite state, the reduced evolution of the register reads

$$\rho(t) = \text{Tr}[U(\rho(t_0) \otimes \varepsilon)U^\dagger] \equiv \xi(\rho_0). \quad (24)$$

This superoperator $\xi(\cdot)$ can be implemented for simulating a noise model in a quantum circuit. The noisy quantum channel describes the nonunitary evolution of the time-varying density state in the Kraus representation

$$\rho(t) = \sum_k E_k \rho(t_0) E_k^\dagger, \quad (25)$$

where E_k satisfy the trace-preserving condition $\sum_k E_k E_k^\dagger = \mathbf{1}$. Since we perform the measurement on the qubits register only at $t = t_f$, imperfections induced by any kind of noise result in fluctuations of the measurement accuracy. In this sense, we shall primarily consider the bit-flip error of measurements in a real quantum computer. Assume the system's noise flips $|0\rangle$ and $|1\rangle$ with probability β . The superoperator for this bit flip noise can be expressed as

$$\xi_{BF}(\rho) = (1-\beta)\rho + \beta X \rho X, \quad (26)$$

where the corresponding Kraus operators are $\{\sqrt{1-\beta}\mathbb{I}, \sqrt{\beta}X\}$, in terms of the identity \mathbb{I} and the Pauli operator X .

Next, we discuss whether the barren plateau [57] phenomenon occurs here. The barren plateau refers to the fact that the gradient of an observable vanishes exponentially as a function of qubits number in a training landscape of VQAs. It has been widely studied in various ansatz of deep circuits [58]. In general, the gradient of an objective function is calculated by mean of the parameter-shift rule [59, 60], expressed as $\partial_{\theta_k} J = \frac{1}{2}[J(\theta_k + \frac{\pi}{2}) - J(\theta_k - \frac{\pi}{2})]$ for an arbitrary trainable parameter θ_k in the circuit. In this sense, we define the aver-

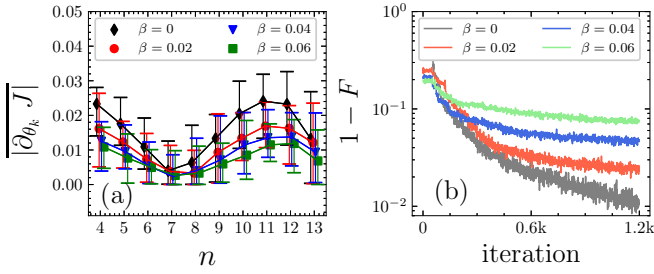


FIG. 6. (a) The average gradient $|\overline{\partial_{\theta_k} J}|$ as a function of the qubit number n and number of layers given by the polynomial function $N_t = 5 \times n$. (b) Infidelities as a function of the training iteration for values of the noise strength $\beta = 0, 0.02, 0.04, 0.06$ based on the SPSA optimizer. Other parameters are equal to those in Fig. 3.

age of the absolute gradient over N_r random initializations

$$\overline{|\partial_{\theta_k} J|} = \sum_{i=1}^{N_r} \frac{1}{2N_r} \left| J_i(\theta_k + \frac{\pi}{2}) - J_i(\theta_k - \frac{\pi}{2}) \right|. \quad (27)$$

Since these three objective functions we proposed in the previous section are all involve the fidelity, we here provide numerical analysis of the average gradients of the fidelity F . Essentially, the probability distribution of qubit states obeys a statistical precision of order $1/\sqrt{N_m}$, and the fidelity defined in Eq. (14) meets the same criteria. The derivative of an observable with respect to an arbitrary trainable θ_k in the circuit is a linear function of the gradient with respect to the corresponding control parameter $f_k = f(k)$ at k -th Trotter step: $\partial_{f_k} J = 2c \cdot \partial_{\theta_k} J$, with c being a real number. Thus, the gradient of the objective function with respect to the control parameter $f(t)$ shares the analytic expression in Eq. (27), see also the detail in Appendix A. Also, we calculate the average gradient Eq. (27) over $N_r = 50$ random initialization of $f(t)$ for various qubit number n , while the Trotter step is taken as a polynomial function as $N_t = \text{ploy}(n)$. In Fig. 6(a), we demonstrate that the *barren plateau* is avoided for the average gradient of a correlating parameter θ_k . The main reason for the absence of *barren plateau* is the reduction of ansatz's expressibility, due to the strong correlation of parameter θ_k depending on the controller $f(t)$ in our method, a common feature with the recent work in Ref. [61]. In this regard, we set measurement shots $N_m = 8192$ for statistical accuracy and energy saving by considering the gradient magnitudes, as shown in Fig. 6(a). Moreover, we apply the optimizer of simultaneous perturbation stochastic approximation (SPSA), which is widely used for solving an optimization problem with statistical noise [62, 63]. In Fig. 6(b), we present the infidelity as a function of the training iteration for $\beta = 0, 0.02, 0.04, 0.06$, where the infidelity for noise-free case ($\beta = 0$) convergent to $\sim 10^{-2}$ which obeys the criteria of $\sim 1/\sqrt{N_m}$. Moreover, the performance of SPSA is compared with various optimizers in Appendix B.

Let us discuss the circuit complexity in terms of the qubits number n and the number of Trotter steps N_t . The whole circuit consists of N_t circuit units that simulate each unitary operation $\hat{U}(dt) = e^{-iHdt}$, as depicted in Fig. 1. In the absence

of θ_1 and θ_2 , the gate number of each circuit unit, including the potential operator $\mathcal{V}(dt)$ and the kinetic-energy operator $\mathcal{T}(dt)$ in real space and momentum space, is $N_{unit} \sim 2n^2$. In addition, the operation of QFT and iQFT requires $\sim n^2/2$ control-phase gates. Consequently, the total number of gates for our ansatz is proportional to a quadratic function of n , yielding $5N_t n^2/2$. To find the minimal-time control on the QC with reasonable precision, one can increase the qubit number n and Trotter step N_t , with exponentially enlarged Hilbert space. But this leads to the quadratic size increase in circuit complexity. Recently, alternative methods inspired by the Grover-Rudolph algorithm [64] are worked out for the quantum state preparation, which are expected to reduce its complexity in this direction.

Finally, we discuss the control problem beyond the quadratic Hamiltonian on which we have focused. For our case study, one can introduce perturbations of the trap, e.g., a time-independent anharmonicity involving an operator x^4 , which is no longer quadratic. Although its exact decomposition into quantum circuits does not exist, one can still approximate the evolution block with arbitrary precision by the Solovay-Kitaev algorithm [65], placing it in the block of $\mathcal{V}_{dt/2}$ before or after the evolution of the quadratic Hamiltonian since it commutes with the harmonic potential operator.

VI. CONCLUSION

To sum up, we propose the GD-based circuit learning to find the time-optimal control problem, the driving of a quantum particle trapped in a time-varying harmonic potential, and figure out its quantum speed limit in relation to the control phase transition. First, we have constructed the digitized quantum circuit of a time-dependent harmonic oscillator using a finite n -qubit register. Second, we have demonstrated that the learning rate of circuit optimization can be accelerated by considering various physical quantities, such as the infidelity, Bures angle, and fidelity susceptibility, as cost functions, thus reducing training iteration. Third, we have established the relation between control phase transition and quantum speed limit. Finally, we have established the error tolerance of our method by considering the presence of measurement errors in a quantum computer. The absence of a barren plateau is further justified in our ansatz, enabling the application of VQAs for a class of tasks that is not affected by the fundamental limitations of NISQ devices. As a heuristic example, we have demonstrated that quantum control can be efficiently simulated and optimized using a NISQ device by combining digital quantum simulation and hybrid circuit learning. Numerical experiments prove that barren plateaus are avoided in the framework.

ACKNOWLEDGMENTS

This work was financially supported by NSFC (12075145), STCSM (Grants No. 2019SHZDZX01-ZX04), EU FET Open Grant EPIQUS (899368), the Basque Government through

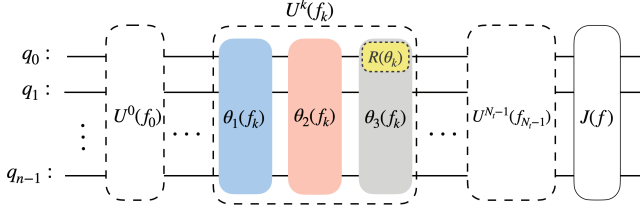


FIG. 7. Schematic illustration of a quantum circuit with Trotter step N_t . Each dashed-block denoted in Fig. 1 presents the implementation of time-evolution $e^{-iH(t)dt}$ with quadratic Hamiltonian $H(t)$ (22). Here, an arbitrary operator $U^k(f_k)$ includes three f_k -correlated variables: $\theta_1(f_k)$, $\theta_2(f_k)$ and $\theta_3(f_k)$. The single-qubit gate with a yellow shadow is used to calculate the gradient of the objective function.

Grant No. IT1470-22, the project grant PID2021-126273NB-I00 funded by MCIN/AEI/10.13039/501100011033 and by “ERDF A way of making Europe” and “ERDF Invest in your Future”, QUANTEK project (KK-2021/00070), and the BRTAQ project (expedient no. KK-2022/00041). HTY acknowledges CSC fellowship (202006890071). X.C. acknowledges ayudas para contratos Ramón y Cajal–2015–2020 (RYC-2017-22482).

Appendix A: The parameter-shift rule

One recipe to find the partial derivative of an objective function $J(\Theta)$ in parametric quantum circuits (PQCs) is known as the parameter-shift rule [59, 60]. In general, the expectation value of an observable \hat{B} as a function of a single parameter θ_k in a circuit is expressed as $J(\theta_k) = \langle \hat{B}(\theta_k) \rangle$. We assume a sequence of unitary operations represented as $U(\theta_k) = U_L U_k(\theta_k) U_R$, for which we have

$$J(\theta_k) = \langle 0 | U_R^\dagger U_k^\dagger(\theta_k) U_L^\dagger \hat{B} U_L U_k(\theta_k) U_R | 0 \rangle = \langle z | \mathcal{M}(\hat{B}, \theta_k) | z \rangle, \quad (\text{A1})$$

where $\mathcal{M}(\hat{B}, \theta_k) = U_k^\dagger(\theta_k) U_L^\dagger \hat{B} U_L U_k(\theta_k)$ and the basis reads $|z\rangle = U_R |0\rangle$. Consider a unitary operator $U_k(\theta_k)$ generated by a Pauli matrix σ_k as $U_k(\theta_k) = \exp(-i\theta_k \sigma_k / 2)$. The gradient of the objective function is defined as

$$\partial_{\theta_k} J(z; \theta_k) = \langle z | \partial_{\theta_k} \mathcal{M}(\hat{B}, \theta_k) | z \rangle = c [\langle z | \mathcal{M}(\theta_k + s) | z \rangle - \langle z | \mathcal{M}(\theta_k - s) | z \rangle] \quad (\text{A2})$$

where coefficient c and shift s are independent of θ_k . The gradient $\partial_{\theta_k} U_k(\theta_k) = -\frac{i}{2} U_k(\theta_k) \sigma_k$, and inserting it to (A1), we have [57] $\partial_{\theta_k} J = -\frac{i}{2} \langle z | U_k^\dagger(\theta_k) [\sigma_k, \hat{B}] U_k(\theta_k) | z \rangle$. The commutation relation, $[\sigma_k, \hat{B}] = i \left(U_k^\dagger(\frac{\pi}{2}) \hat{B} U_k(\frac{\pi}{2}) - U_k^\dagger(-\frac{\pi}{2}) \hat{B} U_k(-\frac{\pi}{2}) \right)$, enables us derive the analytical gradient as [59, 60]:

$$\begin{aligned} \partial_{\theta_k} J &= \frac{1}{2} \langle z | \left[U_k(\theta_k^+) \hat{B} U_k(\theta_k^+) - U_k^\dagger(\theta_k^-) \hat{B} U_k(\theta_k^-) \right] | z \rangle \\ &= \frac{1}{2} [\langle z | \mathcal{M}(\theta_k^+) | z \rangle - \langle z | \mathcal{M}(\theta_k^-) | z \rangle], \end{aligned}$$

with $\theta_k^\pm = \theta_k \pm \pi/2$. The above expression provides an analytical evaluation of the gradient of an objective function involving Pauli operators.

In Fig. 7, we schematically illustrate the deep circuit of our method, which is composed of N_t dashed blocks (refers to N_t Trotter steps). In each unitary operator $U^k(f_k)$, all rotating parameters ($\theta_1, \theta_2, \theta_3$) are f_k -correlated, as detailed in Fig. 1. Let us now select an arbitrary single-qubit gate $R(\theta_k)$, with a gradient obeying the parameter shift rule in Eq. (A3). According to the algorithm in Fig. 1, the rotation θ_k is correlated with f_k as a linear form: $\theta_k = c_1 \cdot f_k$, where c_1 is a real number. Starting with Eq. (A2), we have $\partial_{f_k} J = c[J(f_k + s) - J(f_k - s)] = c[J(\theta_k' + s) - J(\theta_k' - s)]$, where the gradient is independent of the initial angle $\theta_k' = \theta_k / c_1$. Consequently, we find $\partial_{f_k} J = 2c \cdot \partial_{\theta_k} J$, while the shift f_k is $s = \pi/2$. Furthermore, we introduce the notation

$$|\overline{c}| = \sum_{i=1}^{N_r} \frac{1}{2N_r} \left| \frac{\partial_{f_k} J}{\partial_{\theta_k} J} \right|, \quad (\text{A3})$$

where the absolute average value $|\overline{c}|$ over N_r random initialization. In Fig. 8(a), we calculate the average value $|\overline{c}|$ with $N_r = 50$, which is irrelevant to n .

Appendix B: Comparisons of optimizers

In Appendix (B), we compare the performance of several classical optimizers for the same optimization task with statistical errors from a finite number of measurements. We choose widely used optimizers, namely, SLSQP, COBYLA, SPSA, BFQS based on the library of `qiskit`. In Fig. 8(b), we present the infidelity as a function of the training iteration by using various optimizers. The SPSA stands out for its performance in an optimization task in the presence of bit-flip noise.

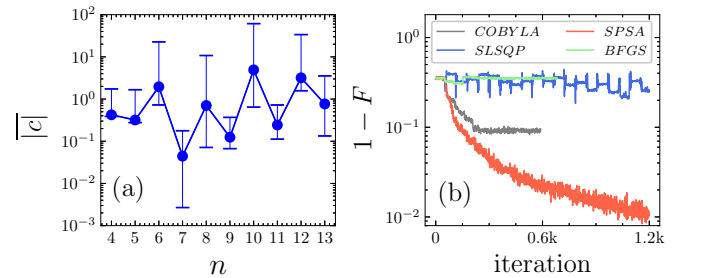


FIG. 8. (a) The coefficient $|\overline{c}|$ as a function of qubit number n . (b) Various training processes for using different optimizers are illustrated. All calculations are proceeded with the parameters $\beta = 0$, $N_m = 8192$, and others in Fig. 3.

- [1] R. P. Feynman, *International Journal of Theoretical Physics* **21**, 467 (1982).
- [2] B. P. Lanyon, C. Hempel, D. Nigg, M. Müller, R. Gerritsma, F. Zähringer, P. Schindler, J. T. Barreiro, M. Rambach, G. Kirchmair, M. Hennrich, P. Zoller, R. Blatt, and C. F. Roos, *Science* **334**, 57 (2011).
- [3] Y. Salathé, M. Mondal, M. Oppliger, J. Heinsoo, P. Kurpiers, A. Potočnik, A. Mezzacapo, U. Las Heras, L. Lamata, E. Solano, S. Filipp, and A. Wallraff, *Phys. Rev. X* **5**, 021027 (2015).
- [4] C. Hempel, C. Maier, J. Romero, J. McClean, T. Monz, H. Shen, P. Jurcevic, B. P. Lanyon, P. Love, R. Babbush, A. Aspuru-Guzik, R. Blatt, and C. F. Roos, *Phys. Rev. X* **8**, 031022 (2018).
- [5] P. J. J. O'Malley, R. Babbush, I. D. Kivlichan, J. Romero, J. R. McClean, R. Barends, J. Kelly, P. Roushan, A. Tranter, N. Ding, B. Campbell, Y. Chen, Z. Chen, B. Chiaro, A. Dunsworth, A. G. Fowler, E. Jeffrey, E. Lucero, A. Megrant, J. Y. Mutus, M. Neeley, C. Neill, C. Quintana, D. Sank, A. Vainsencher, J. Wenner, T. C. White, P. V. Coveney, P. J. Love, H. Neven, A. Aspuru-Guzik, and J. M. Martinis, *Phys. Rev. X* **6**, 031007 (2016).
- [6] C. Gogolin, M. P. Müller, and J. Eisert, *Phys. Rev. Lett.* **106**, 040401 (2011).
- [7] A. Polkovnikov, K. Sengupta, A. Silva, and M. Vengalattore, *Rev. Mod. Phys.* **83**, 863 (2011).
- [8] M. C. Bañuls, R. Blatt, J. Catani, A. Celi, J. I. Cirac, M. Dalmonte, L. Fallani, K. Jansen, M. Lewenstein, S. Montangero, C. A. Muschik, B. Reznik, E. Rico, L. Tagliacozzo, K. Van Acoleyen, F. Verstraete, U.-J. Wiese, M. Wingate, J. Zakrzewski, and P. Zoller, *The European Physical Journal D* **74**, 165 (2020).
- [9] L. García-Álvarez, I. L. Egusquiza, L. Lamata, A. del Campo, J. Sonner, and E. Solano, *Phys. Rev. Lett.* **119**, 040501 (2017).
- [10] Z. Luo, Y.-Z. You, J. Li, C.-M. Jian, D. Lu, C. Xu, B. Zeng, and R. Laflamme, *npj Quantum Information* **5**, 53 (2019).
- [11] J. Preskill, *Quantum* **2**, 79 (2018).
- [12] Y. Salathé, M. Mondal, M. Oppliger, J. Heinsoo, P. Kurpiers, A. Potočnik, A. Mezzacapo, U. Las Heras, L. Lamata, E. Solano, S. Filipp, and A. Wallraff, *Phys. Rev. X* **5**, 021027 (2015).
- [13] E. A. Martinez, C. A. Muschik, P. Schindler, D. Nigg, A. Erhard, M. Heyl, P. Hauke, M. Dalmonte, T. Monz, P. Zoller, and R. Blatt, *Nature* **534**, 516 (2016).
- [14] C. Kokail, C. Maier, R. van Bijnen, T. Brydges, M. Joshi, P. Jurcevic, C. A. Muschik, P. Silvi, R. Blatt, C. F. Roos, and P. Zoller, *Nature* **569**, 355 (2019).
- [15] E. Farhi, J. Goldstone, and S. Gutmann, arXiv preprint arXiv:1411.4028 (2014).
- [16] A. Pesah, M. Cerezo, S. Wang, T. Volkoff, A. T. Sornborger, and P. J. Coles, *Phys. Rev. X* **11**, 041011 (2021).
- [17] A. B. Magann, C. Arenz, M. D. Grace, T.-S. Ho, R. L. Kosut, J. R. McClean, H. A. Rabitz, and M. Sarovar, *PRX Quantum* **2**, 010101 (2021).
- [18] M. Suzuki, *Communications in Mathematical Physics* **51**, 183 (1976).
- [19] M. Suzuki, *Proceedings of the Japan Academy, Series B* **69**, 161 (1993).
- [20] S. Lloyd, *Science* **273**, 1073 (1996).
- [21] M. Suzuki, *Physics Letters A* **146**, 319 (1990).
- [22] U. Las Heras, U. Alvarez-Rodriguez, E. Solano, and M. Sanz, *Phys. Rev. Lett.* **116**, 230504 (2016).
- [23] S. McArdle, X. Yuan, and S. Benjamin, *Phys. Rev. Lett.* **122**, 180501 (2019).
- [24] Y.-X. Liu, J. Hines, Z. Li, A. Ajoy, and P. Cappellaro, *Phys. Rev. A* **102**, 010601 (2020).
- [25] A. Bolens and M. Heyl, *Phys. Rev. Lett.* **127**, 110502 (2021).
- [26] T. Fösel, P. Tighineanu, T. Weiss, and F. Marquardt, *Phys. Rev. X* **8**, 031084 (2018).
- [27] M. Bukov, *Phys. Rev. B* **98**, 224305 (2018).
- [28] F. Albarrán-Arriagada, J. C. Retamal, E. Solano, and L. Lamata, *Phys. Rev. A* **98**, 042315 (2018).
- [29] A. Peruzzo, J. McClean, P. Shadbolt, M.-H. Yung, X.-Q. Zhou, P. J. Love, A. Aspuru-Guzik, and J. L. O'Brien, *Nature Communications* **5**, 4213 (2014).
- [30] J. R. McClean, J. Romero, R. Babbush, and A. Aspuru-Guzik, *New Journal of Physics* **18**, 023023 (2016).
- [31] G. S. Giuliano Benenti, arXiv , 0709.1704 (2007).
- [32] P. J. Ollitrault, G. Mazzola, and I. Tavernelli, *Phys. Rev. Lett.* **125**, 260511 (2020).
- [33] M. Bukov, A. G. R. Day, D. Sels, P. Weinberg, A. Polkovnikov, and P. Mehta, *Phys. Rev. X* **8**, 031086 (2018).
- [34] X. Chen, A. Ruschhaupt, S. Schmidt, A. del Campo, D. Guéry-Odelin, and J. G. Muga, *Phys. Rev. Lett.* **104**, 063002 (2010).
- [35] Y. Li, L.-A. Wu, and Z. D. Wang, *Phys. Rev. A* **83**, 043804 (2011).
- [36] J. García-Ripoll, A. Ruiz-Chamorro, and E. Torrontegui, *Phys. Rev. Applied* **14**, 044035 (2020).
- [37] R. Kosloff, *The Journal of Physical Chemistry* **92**, 2087 (1988).
- [38] D. Stefanatos, J. Ruths, and J.-S. Li, *Phys. Rev. A* **82**, 063422 (2010).
- [39] K. Hoffmann, P. Salamon, Y. Rezek, and R. Kosloff, *EPL (Europhysics Letters)* **96**, 60015 (2011).
- [40] T.-Y. Huang, B. A. Malomed, and X. Chen, *Chaos: An Interdisciplinary Journal of Nonlinear Science* **30**, 053131 (2020).
- [41] L. Dupays, D. C. Spierings, A. M. Steinberg, and A. del Campo, *Phys. Rev. Research* **3**, 033261 (2021).
- [42] S. Deffner and S. Campbell, *Journal of Physics A: Mathematical and Theoretical* **50**, 453001 (2017).
- [43] T. Caneva, M. Murphy, T. Calarco, R. Fazio, S. Montangero, V. Giovannetti, and G. E. Santoro, *Phys. Rev. Lett.* **103**, 240501 (2009).
- [44] K. Funo, J.-N. Zhang, C. Chatou, K. Kim, M. Ueda, and A. del Campo, *Phys. Rev. Lett.* **118**, 100602 (2017).
- [45] S. Campbell and S. Deffner, *Phys. Rev. Lett.* **118**, 100601 (2017).
- [46] L. Mandelstam and I. Tamm, *J. Phys. USSR* **9**, 249 (1945).
- [47] N. Margolus and L. B. Levitin, *Physica D: Nonlinear Phenomena* **120**, 188 (1998).
- [48] G. Ness, M. R. Lam, W. Alt, D. Meschede, Y. Sagi, and A. Alberti, *Science Advances* **7**, eabj9119 (2021).
- [49] J. Anandan and Y. Aharonov, *Phys. Rev. Lett.* **65**, 1697 (1990).
- [50] A. Uhlmann, *Physics Letters A* **161**, 329 (1992).
- [51] S. Deffner and E. Lutz, *Journal of Physics A: Mathematical and Theoretical* **46**, 335302 (2013).
- [52] W.-L. You, Y.-W. Li, and S.-J. Gu, *Phys. Rev. E* **76**, 022101 (2007).
- [53] S.-J. Gu, H.-M. Kwok, W.-Q. Ning, and H.-Q. Lin, *Phys. Rev. B* **77**, 245109 (2008).
- [54] S.-J. GU, *International Journal of Modern Physics B* **24**, 4371 (2010), <https://doi.org/10.1142/S0217979210056335>.
- [55] P. T. Boggs and J. W. Tolle, *Sequential Quadratic Programming*, Vol. 4 (Cambridge University Press, 1995) p. 1–51.

- [56] P. Virtanen, R. Gommers, T. E. Oliphant, and etc., *Nature Methods* **17**, 261 (2020).
- [57] J. McClean, S. Boixo, V. Smelyanskiy, R. Babbush, and H. Neven, *Nature Communications* **9**, 4812 (2018).
- [58] M. Cerezo, A. Arrasmith, R. Babbush, S. C. Benjamin, S. Endo, K. Fujii, J. R. McClean, K. Mitarai, X. Yuan, L. Cincio, *et al.*, *Nature Reviews Physics* **3**, 625 (2021).
- [59] K. Mitarai, M. Negoro, M. Kitagawa, and K. Fujii, *Phys. Rev. A* **98**, 032309 (2018).
- [60] M. Schuld, V. Bergholm, C. Gogolin, J. Izaac, and N. Killoran, *Phys. Rev. A* **99**, 032331 (2019).
- [61] Z. Holmes, K. Sharma, M. Cerezo, and P. J. Coles, *PRX Quantum* **3**, 010313 (2022).
- [62] J. C. Spall, *Johns Hopkins Apl Technical Digest* **19**, 482 (1998).
- [63] L. Bottou, *Proceedings of COMPSTAT'2010*, edited by Y. Lechevallier and G. Saporta (Physica-Verlag HD, Heidelberg, 2010) pp. 177–186.
- [64] G. Marin-Sanchez, J. Gonzalez-Conde, and M. Sanz, arXiv preprint arXiv:2111.07933 (2021).
- [65] A. Y. Kitaev, *Russian Mathematical Surveys* **52**, 1191 (1997).